ADVANCED FUNCTIONAL MATERIALS
www.afm-journal.de

Controlled Stepwise Wet Etching of Polycrystalline Mo Nanowires

*Khakimjon Saidov, Ivan Erofeev, Zainul Aabdin, Antoine Pacco, Harold Philipsen, Antony Winata Hartanto, Yifan Chen, Hongwei Yan, Weng Weei Tjiu, Frank Holsteyns, and Utkur Mirsaidov**

With the persistent downscaling of integrated circuits, molybdenum (Mo) is currently considered a potential replacement for copper (Cu) as a material for metal interconnects. However, fabricating metal nanostructures with critical dimensions of the order of 10 nm and below is challenging. This is because the very high density of grain boundaries (GBs) results in highly non-uniform surface profiles during direct wet etching. Moreover, wet etching of Mo with conventional aqueous solutions is problematic, as products of Mo oxidation have different solubility in water, which leads to increased surface roughness. Here, a process is shown for achieving a stable and uniform soluble surface layer of Mo oxide by wet oxidation with H_2O_2 dissolved in IPA at −20 °C. The oxide layer is then selectively dissolved, and by repeating the oxidation and dissolution multiple times, a uniform etch profile is demonstrated with a fine control over the metal recess. Ultimately, this presents a method of precise and uniform wet etching for Mo and other metals needed to fabricate complex nanostructures that are critical in developing next-generation electronic devices.

1. Introduction

The ever-growing demand for high-performance and power-efficient microelectronic devices has driven the semiconductor industry to downscale the transistors and metal interconnects.[1,2] The interconnects are the nanocrystalline metal nanowires (NWs) connecting the transistors, and copper (Cu) has been used as the core metal of interconnects over the past two decades.[3–5] However, as the critical dimensions of NWs decrease below 10 nm, the resistivity of Cu becomes much higher than in the bulk due to the long electron mean free path.[6,7] Thus, there is a strong need for alternative metals, such as molybdenum (Mo), cobalt (Co), and ruthenium (Ru), that outperform Cu at the sub-10 nm scale[8–10]. Among these metals, Mo is the most promising candidate because, in addition to its lower nanoscale resistivity versus Cu, Mo also allows for a barrier-less process, saving more room for the core metal.[6,7]

At the nanoscale, the electrical resistivity of metal NWs is strongly affected by the electron scattering from the surface and grain boundaries (GBs).[1,4,6,11–15] Chemical wet etching is the fabrication step that affects uniformity and surface roughness of metal NWs the most, so it is imperative to achieve a smooth (isotropic), atomic-level

K. Saidov, U. Mirsaidov
Department of Physics
National University of Singapore
Singapore 117551, Singapore
E-mail: mirsaidov@nus.edu.sg

K. Saidov, I. Erofeev, A. W. Hartanto, Y. Chen, H. Yan, U. Mirsaidov
Centre for BioImaging Sciences
Department of Biological Sciences
National University of Singapore
Singapore 117557, Singapore

K. Saidov, I. Erofeev, A. W. Hartanto, U. Mirsaidov
Centre for Advanced 2D Materials
National University of Singapore
Singapore 117546, Singapore

Z. Aabdin, W. W. Tjiu
Institute of Materials Research and Engineering (IMRE)
Agency for Science
Technology and Research (A*STAR)
Singapore 138634, Singapore

A. Pacco, H. Philipsen, F. Holsteyns
IMEC
Kapeldreef 75, Leuven B-3001, Belgium

U. Mirsaidov
Department of Materials Science and Engineering
National University of Singapore
Singapore 117575, Singapore

The ORCID identification number(s) for the author(s) of this article can be found under https://doi.org/10.1002/adfm.202310838

DOI: 10.1002/adfm.202310838

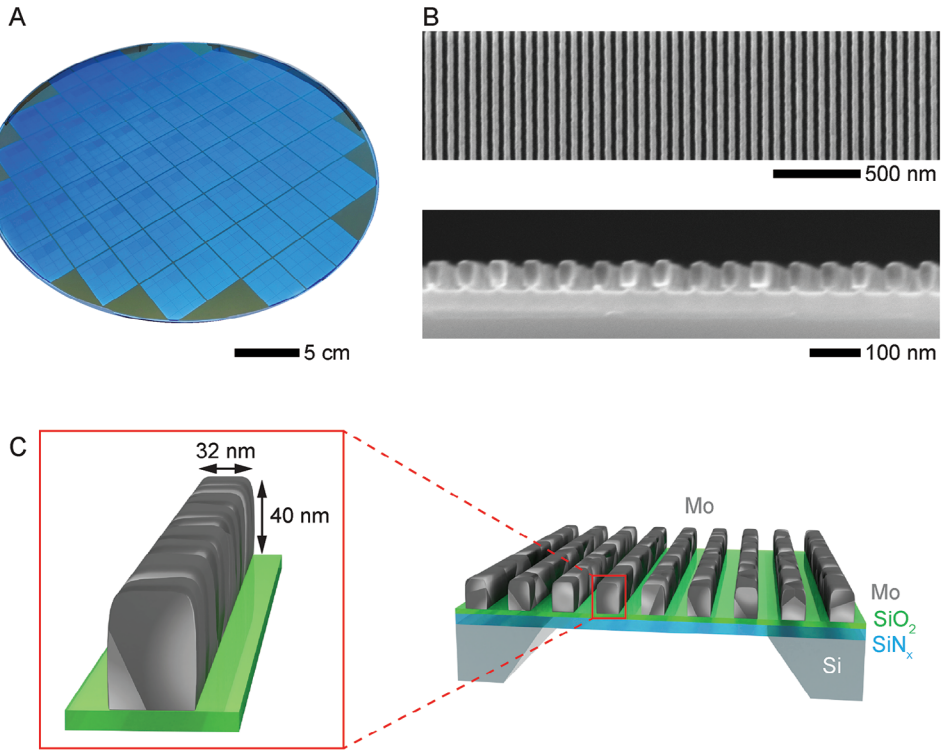

Figure 1. Overview of Mo NWs. A) Nanocrystalline Mo NWs with rectangular cross-sections were fabricated on a 300-mm Si wafer (Figure S1, Supporting Information). B) Top-down and side-view SEM images of Mo NWs on a SiO_2/SiN_x film. C) Schematic of the nanocrystalline Mo NWs on a SiO_2/SiN_x film.

controlled, and selective etching process.[16] Nevertheless, controlled and uniform wet etching of nanocrystalline Mo NWs is challenging because of the varying etching rates for different grain orientations and GBs. Hence, understanding and developing reliable wet etching processes for nanocrystalline metals such as Mo is critical for the future fabrication of semiconductor devices. While direct wet etching of single nanocrystals has been extensively studied and fairly well understood,[17–19] the etching process for nanocrystalline metals is more complex and difficult to control due to the effects of different grain orientations and GBs at the surface.[20–23] A two-step approach involving self-limiting metal oxidation followed by selective oxide dissolution has been proposed for better etching control.[16,24] Nonetheless, self-limiting wet oxidation of Mo has not yet been achieved, with only thermal oxidation currently available.[16]

Here, we explored the dynamics of wet etching of polycrystalline Mo NWs with hydrogen peroxide (H_2O_2) solutions. We tracked the direct etching of the Mo NWs with 1% (v/v) H_2O_2 aqueous solution using in situ liquid phase transmission electron microscopy (LP-TEM)[19,23,25] and observed the formation of etching non-uniformities, in particular at the GBs. We show that the etching profile of Mo NWs becomes significantly more uniform when water is substituted with isopropyl alcohol (IPA) as a solvent. Furthermore, we demonstrate the first instance of wet chemical oxidation of Mo for the two-step approach by adjusting the reaction temperature, thus reducing the Mo oxide dissolution rate to a negligible rate. We show that this process can be repeated in multiple cycles for the uniform and controllable recess of the Mo NWs.

2. Results and Discussion

To observe the etching process of a natural nanocrystalline Mo surface, we used wafer-scale patterned Mo NWs similar to the metal lines envisioned to serve as interconnects in future microelectronics components (**Figure 1**A,B). Each NW has a rectangular cross-section with a width of ≈32 nm and a height of ≈40 nm (Figure 1C). We chose an aqueous hydrogen peroxide (H_2O_2) solution as a chemical etchant, which is the most commonly used etchant for Mo.[26,27] Before the etching, Mo NWs were smooth and straight, featuring only a minor waviness (**Figure 2**A). The selected area electron diffraction (SAED) pattern of the NWs corresponds to pure Mo metal with ⟨110⟩ texture, and we estimated the average grain size of ≈22 nm from TEM images. Figure 2B shows the same NWs after etching in an aqueous H_2O_2 solution (1% v/v) for 45 s at room temperature. Compared to their initial state in Figure 2A, the mean NW width decreased from ≈31 to ≈21 nm (corresponding to an etching rate of ≈0.1 nm s^{-1}). However, the NW surfaces are now rough, and individual grains are faceted, which is a clear sign of anisotropic etching. Moreover, we observe multiple pits and grooves at grain surfaces and GBs, which indicate an enhanced etching rate at surface defects. The SAED pattern in Figure 2B shows that no new crystalline phases form during the etching process.

To better understand how the NW surface evolves during the etching, we tracked the entire process in real-time with LP-TEM (**Figure 3**).[25,28–30] The plot of the width of Mo NWs (Figure 3B) extracted from the in situ TEM images series (Figure 3C; Video S1, Supporting Information) shows the gradual width recess for

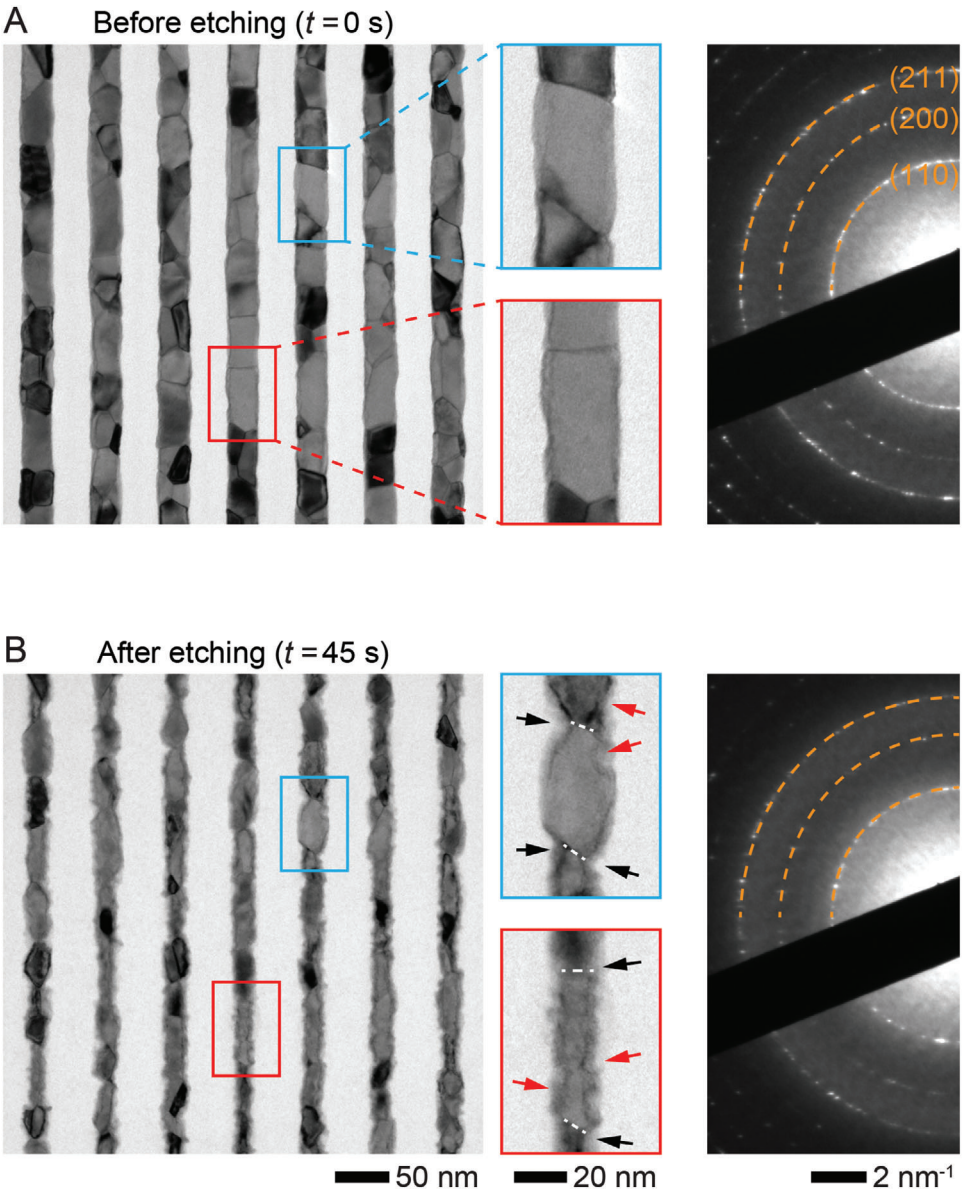

Figure 2. Direct wet chemical etching of Mo NWs. TEM images of Mo NWs A) before and B) after 45-s-long wet etching in an aqueous H_2O_2 solution (1% v/v). Red and black arrows indicate the etching of grain sidewalls and GBs, respectively. The three diffraction rings in (A,B) correspond to (110), (200), and (211) planes of metallic Mo. [Correction added on December 20, 2023, after first online publication: figure 2 has been exchanged in this version.]

four metal NWs, where the etching rate, defined as the rate of the NW width reduction, remained almost constant at ≈0.02 nm s^{-1} throughout the etching. However, a closer examination of the selected area in Figure 3D reveals that some pits formed at the GBs at the early stage (Figure 3D: $t - t_0 = 0$–130 s), suggesting that GBs are more susceptible to etching than the sidewalls. As the reaction proceeds, some of these pits also developed faceted edges (Figure 3D: $t - t_0 = 280$–370 s).

Unlike single-crystal nanoparticles that are often synthesized and enclosed by low-index facets, the NWs are patterned from a thin metal film with reactive ion etching (RIE) that has no regard for crystallography. Since the grain orientation in the film is largely random, the exposed surfaces of NWs are also random, with a higher chance of being high-index facets. Metal atoms on such surfaces have weaker connections to their neighbors than on low-index facets because they have a lower coordination number (CN) and are, therefore, less stable. During etching, the lowest-CN atoms leave the surface first, so the etching naturally starts at the grain corners, that is, at the GB.[31,32] Once a stable low-index plane is exposed, the etching slows down, but the corner atoms are still the least stable because of the lower CN. As a result, many grains develop faceted surfaces and maintain them throughout the etching process. In Figure 2B, we also observe multiple faceted pits along grain surfaces away from GBs, which likely grow from surface defects that also feature atoms with low CN.[27,32] Note that for a stable low-index facet to appear, it has to

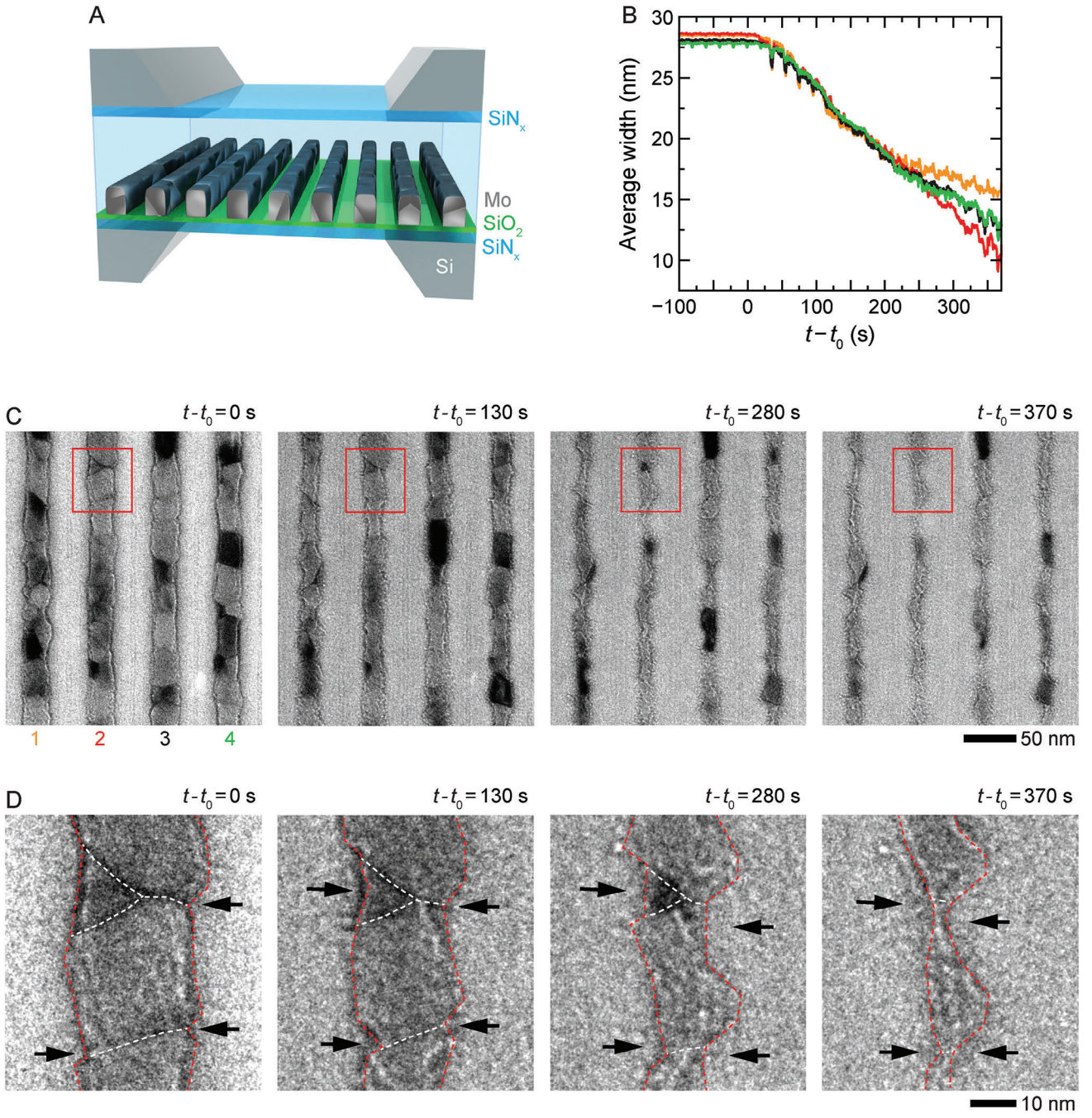

Figure 3. In situ TEM imaging of wet etching of the Mo NWs. A) Schematic of liquid cell used for in situ TEM imaging. Here, the etching solution is encapsulated between two Si chips with SiN_x windows, with Mo NWs patterned on the bottom chip. B) Changes in the average widths of the four Mo NWs obtained from C) TEM image series of the NWs undergoing the etching (Video S1, Supporting Information). t_0 is the timepoint at which etching starts. D) Enlarged view of selected regions showing accelerated etching at GBs and faceting at grain surfaces. Dashed red and white lines mark grain sidewalls and GBs, respectively, while black arrows indicate the areas that are etching faster.

be nearly perpendicular to the etching direction. If a grain orientation is inappropriate, the etching will proceed with the unstable high-index facet exposed, resulting in a faster overall etching rate and likely a rougher surface. Eventually, this anisotropic facet-dependent etch rate leads to an uneven metal recess. It is unavoidable when using direct wet etching of nanocrystalline metals, though the anisotropy can be slightly suppressed by carefully selecting the etching solution composition for each metal.[24,33,34]

In the case of direct wet etching of Mo, there is an additional factor at play. The etching with H_2O_2 aqueous solution proceeds via sequential Mo oxidation to MoO_2 (Mo^{4+} oxidation state) and MoO_3 (Mo^{6+} oxidation state).[26,27] The latter is soluble in

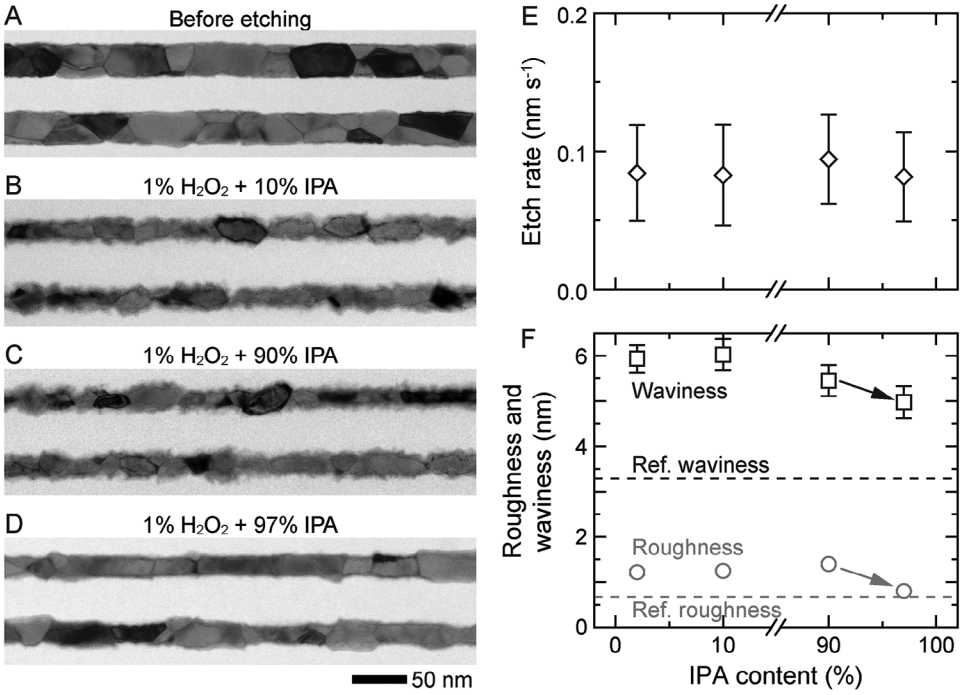

Figure 4. Influence of IPA on wet etching uniformity. TEM images of Mo NWs A) before and after 45-s etching in the H_2O_2 solutions (1% (v/v)) containing B) 10, C) 90, and D) 97% (v/v) IPA. E) The etch rates and F) roughness and waviness plots obtained from TEM images taken after 45 s of etching in 1% (v/v) H_2O_2 solutions with different IPA concentrations. Reference (Ref.) waviness and roughness refer to the waviness and roughness of original unetched NWs.

water and, therefore, leaves the NW surface, while MoO_2 with Mo^{4+} stays on the metal surface, waiting to be oxidized further. The dynamics of this process depend on the relative rates of Mo^0/Mo^{4+} oxidation and Mo^{6+} dissolution. If the oxidation rate is higher, then virtually no MoO_2 is ever present on the metal surface because it has enough time to oxidize completely and uniformly before dissolving into the solution. On the other hand, if the dissolution rate is higher, the surface always has some intermediate Mo^{4+} oxide. In this case, the oxidation front can become non-uniform due to transient MoO_2 islands, especially at the high-index surfaces of grains.

At 1% (v/v) of H_2O_2, the etching rate is already relatively high, so the oxidation/dissolution ratio control is best achieved by varying the solubility of MoO_3 in the etching solution. MoO_3 is sparingly soluble in water with ≈4.90 g L^{-1} at 28 °C,[35,36] but it is insoluble in nonpolar organic solvents such as isopropyl alcohol (IPA) or acetone, which cannot effectively interact with ionic compounds like MoO_3.[37,38] We selected IPA to gradually replace the water in the etching solution and, therefore, control MoO_3 solubility, as it is compatible and miscible with both water and H_2O_2. If all the water is replaced with IPA, it can potentially stop the dissolution of MoO_3 entirely. However, since we start with 30% H_2O_2 aqueous solution (see Experimental Section), we can effectively reduce the final water concentration in the etching solution from 99% (1% (v/v) H_2O_2 in water) to ≈2% (1% (v/v) H_2O_2 in IPA), which means a 50-fold reduction in the dissolution rate of MoO_3. **Figure 4** shows the Mo NWs after 45 s of room-temperature etching with 1% (v/v) H_2O_2 solutions containing 10 to 97% of IPA. The NW surface after etching with 10–90% of IPA (Figure 4B,C) is very similar to that after etching with H_2O_2 in pure water (Figure 2A). However, with only 2% water, the metal surface looks much smoother and cleaner (Figure 4D), while the overall etching rate remained unchanged at different IPA concentrations (Figure 4E).

We characterized the surface roughness using a modified line edge roughness (LER) method,[39–42] separating the small-scale roughness (at the scale of 1–2 nm and below, caused by fast-etching in defects and MoO_2 masking, below referred to as simply roughness) and the large-scale surface "waviness" (caused by crystallographic anisotropy). Figure 4F compares both surface roughness and waviness after etching with varying IPA concentrations, showing no significant variation of both parameters from 0% to 90% of IPA and a notable reduction of roughness at 97% IPA (as indicated by arrows in Figure 4F). This result confirms the discussed effect of MoO_3 dissolution rate on the etching uniformity.

Even though this is already a big improvement, the metal surface roughness is still higher than that of the initial NW (Figure 4F). Additionally, the direct etching approach relies on the precise timing to control the metal recess. To achieve a smoother surface and a more reliable recess control, we have to implement a two-step approach: form a stable, uniform, and self-limiting oxide layer and then selectively dissolve it. This means that we need to completely stop the dissolution of MoO_3 in the H_2O_2–IPA solution. Removing the remaining 2% of water is the straightforward way, but it requires the use of 100% H_2O_2, which is hazardous and generally impractical. Alternatively, we can make use of the temperature dependence of the MoO_3 solubility. As

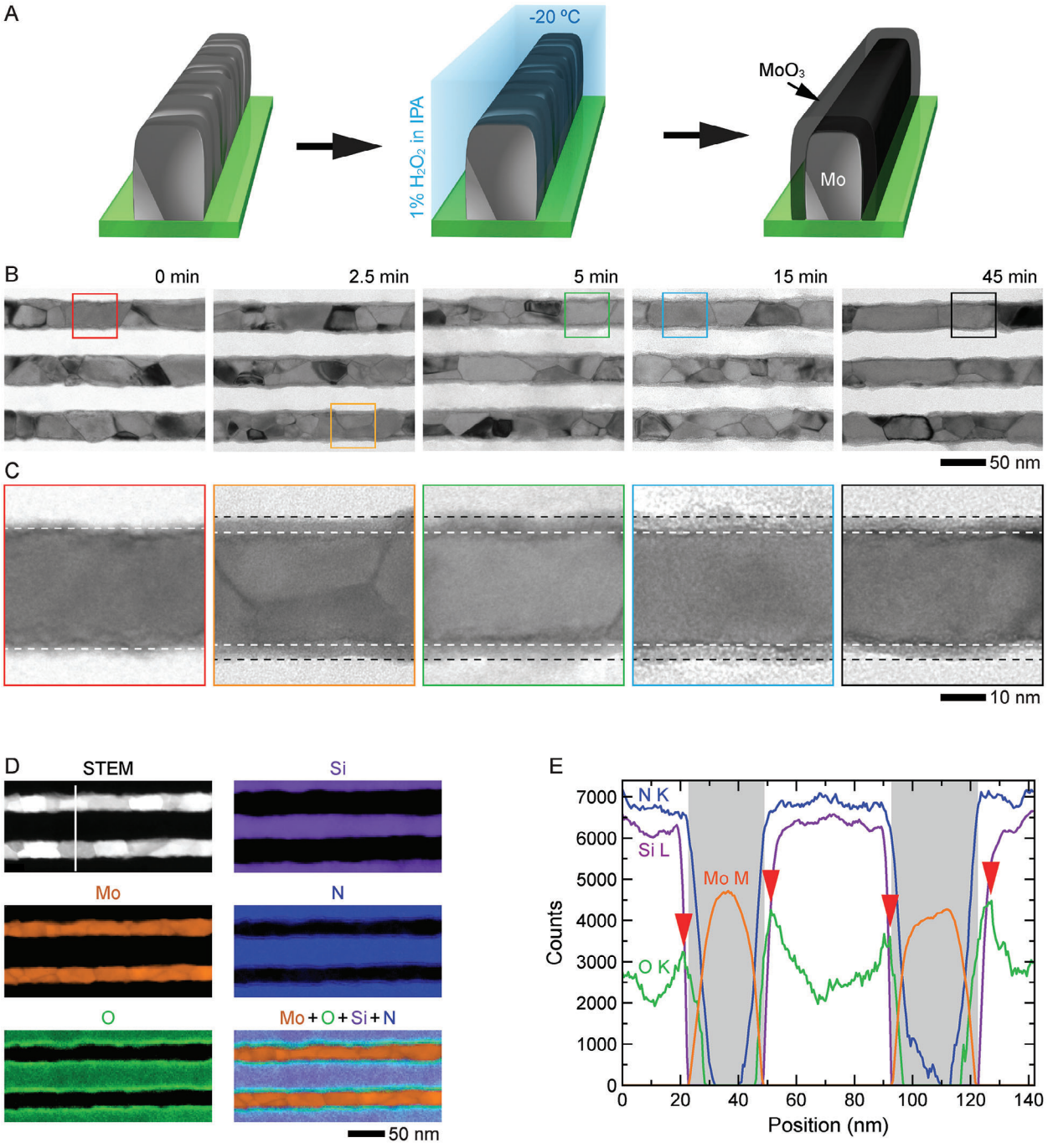

Figure 5. Low-temperature wet oxidation of Mo NWs. A) Schematic showing the oxidation process of Mo NWs in a 1% (v/v) H_2O_2 solution in IPA (97% v/v) at −20 °C. B) TEM images of the Mo NWs after oxidation for 0–45 min. C) Enlarged views from the selected regions in (B). The dashed white and black lines indicate the positions of the starting Mo surface and the formed Mo oxide layers, respectively. D) STEM image and the corresponding EELS maps of the Mo NWs after the 45-min-long low-temperature oxidation in H_2O_2 (in IPA) solution. E) Elemental line profile along the white line in (D). Red arrows highlight O peaks associated with the Mo oxide layer on the NW surface.

mentioned above, at 28 °C it is ≈4.90 g L^{-1} but drops to 1.07 g L^{-1} at 18 °C,[35,36] and this trend can be extended to 0 °C for 1% H_2O_2 in pure water or even below that, if IPA is present in the solution.[43] We tested 1% H_2O_2 in pure water at 0 °C, but it did not lead to a stable oxide layer (Figure S2, Supporting Information). Ultimately, we used a 1% H_2O_2 solution with the highest possible concentration of IPA at 97%, similar to the previous experiment, to treat Mo NWs in a freezer at −20 °C. The process is schematically shown in **Figure 5**A: instead of being etched, the NW is covered by a uniform layer. The thickness of this layer ≈4 nm does not depend on the reaction time (Figure 5B,C: t = 2.5–45 min). Scanning TEM (STEM) electron

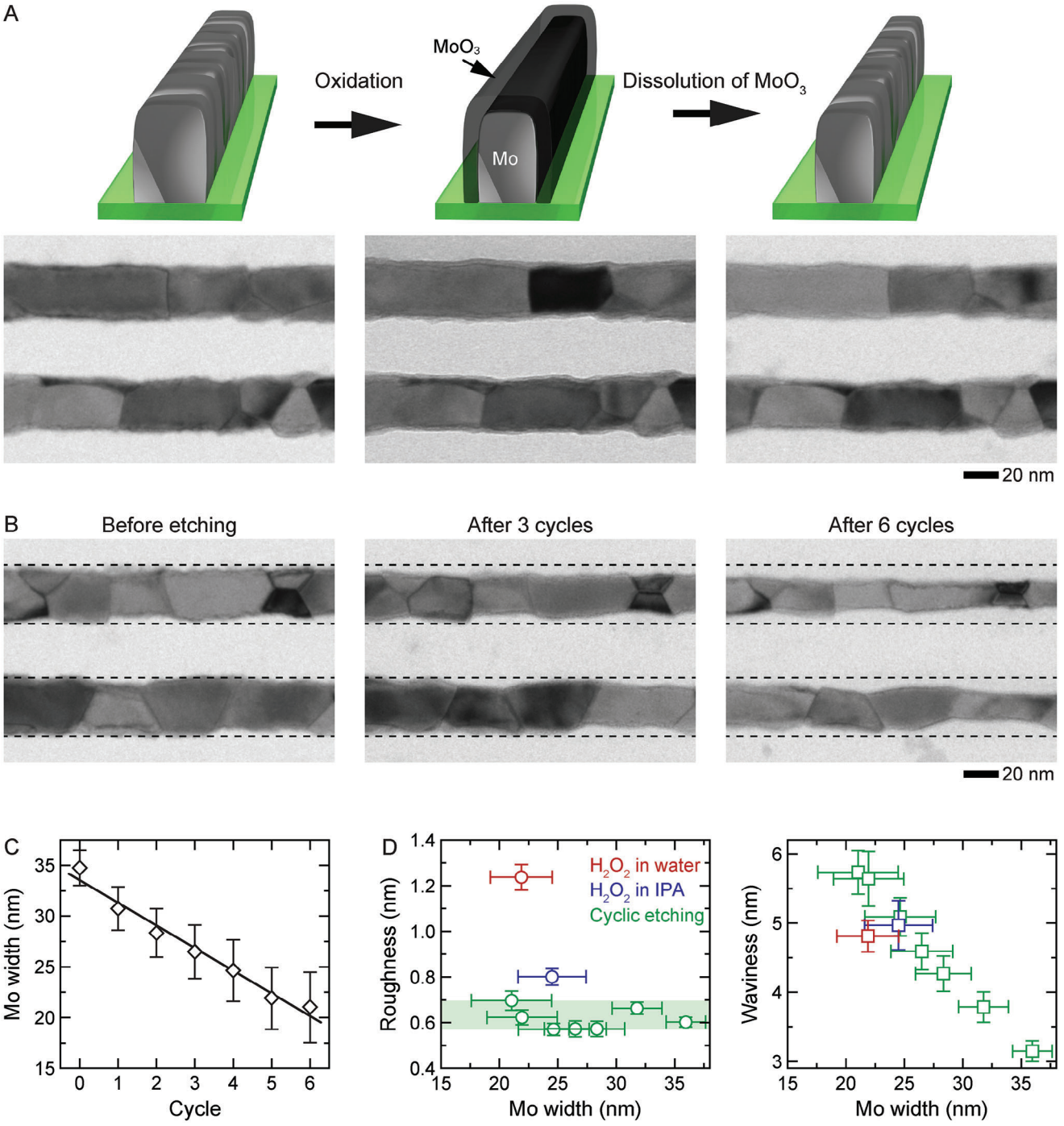

Figure 6. Digital wet etching of Mo NWs through low-temperature oxidation and dissolution. A) Schematic and TEM images of the Mo NWs during one cycle of the digital etching via the formation and dissolution of the Mo oxide. The Mo oxide formed by oxidation of the Mo NWs in the 1% (v/v) H_2O_2 in IPA at −20 °C for 5 min, and the Mo oxide was selectively dissolved in deionized water for 5 min. B) TEM images showing the recess of the same Mo NWs during multiple cycles of the digital etching. The dashed black lines indicate the positions of the starting Mo surface. The change of C) the average width, D) roughness, and waviness of the Mo NWs during direct etching and multiple cycles of the digital etching. The black line in (C) is the linear fit to the data, which yields an etch rate of 2.2 nm per digital etching cycle.

energy loss spectroscopy (EELS) results (Figure 5D,E) show a strong oxygen and a weak Mo signal from this layer, indicating that this is a Mo oxide layer. After a brief treatment with pure deionized (DI) water at room temperature, the NW surface was rendered clean, confirming this to be the water-soluble MoO_3 layer.

Having achieved a stable Mo oxide layer with low-temperature wet oxidation at −20 °C, we then explored how the NWs evolve during cyclic digital etching. **Figure** 6A presents a schematic representation and corresponding TEM images of one digital etching cycle. Here, Mo NWs were oxidized using the solution of 1% (v/v) H_2O_2 solution with 97% IPA for 5 min at −20 °C as presented above (step 1: oxidation), followed by a complete dissolution of the oxide layer in deionized water (step 2: dissolution). We repeated this process multiple times (Figure 6B), and the average NW width consistently decreased by ≈2.2 nm each cycle (Figure 6C). After each cycle, we measured the roughness and waviness of Mo NWs and compared them to the results of direct etching with 1% H_2O_2 in pure water and with 97% IPA at room temperature (Figure 6D). The surface roughness is substantially lower than after the direct etching with 97% IPA solution at room temperature, and importantly, it remains nearly the same over many oxidation-etching cycles. The surface waviness increases each cycle and exceeds that for direct etching at the same NW width. It means that the long oxidation phase is slightly more sensitive to crystallographic anisotropy than fast direct etching. We attribute these differences to the thermodynamic equilibrium established between the oxide layer and the underlying metal surface when the former stays intact, in contrast to the more "kinetic" reaction during the direct etching process.

In this work, we have focused on Mo as a case study due to its emerging importance as a material for metal interconnects in advanced integrated circuits. However, the fundamental principles and insights gained from our study on etching can be applied to other metals. One of the key challenges we addressed here is that oxides with different oxidation states have different solubility in the etching solution, which is also the case with some other transition metals (e.g., Co, W, Ru, and Os). More general issues, such as crystal anisotropy and high density of GBs, are commonly encountered in the wet etching of all nanocrystalline metals used in microelectronics, including Cu and Al. Of course, each of these metals has its unique properties and chemistry, but the underlying approach of engineering the etching environment to control oxide layer formation and dissolution is a general concept. The key is to identify the appropriate etchant solutions and tailor the conditions for each specific metal.

3. Conclusion

Our direct observations of wet chemical etching of Mo metal NWs in H_2O_2 reveal that because of varying etch rates along the different crystallographic orientations and associated grain boundaries, direct etching of polycrystalline metals fails to produce uniform etch profiles at the nanoscale. We show that this issue can be overcome by a synergetic approach to manipulating the oxidation product solubility: replacing water with IPA in the etching solution reduces the dissolution rate of MoO_3, enabling smooth direct etching, and also allows to decrease the liquid solution temperature to −20 °C to prevent any premature dissolution of the oxide layer that forms on the surface. This enabled us to realize a cyclic "digital" process with solution-based oxidation and dissolution steps, resulting in a great recess control and a highly uniform etching profile with an atomically smooth surface. Importantly, this approach can be readily extended for precise nanoscale wet etching of other metals, and the insights here provide a direct route to enhancing and refining nanofabrication processes in the development of advanced electronic devices.

4. Experimental Section

Fabrication of Mo nanowires: First, a 40-nm-thick SiN_x film was grown using low-pressure chemical vapor deposition (LPCVD) on both the front and back side of a 300-mm Si substrate wafer (the back side SiN_x film serves as a hard mask for patterning the windows and groves for TEM chips, while the front side SiN_x layer acts as an electron-transparent membrane). Next, a 10-nm-thick SiO_2 layer was deposited on the front side as an etch-stop-layer (ESL), followed by a deposition of 50-nm-thick Mo film on top of the ESL using physical vapor deposition (PVD) at 280 °C. The film was annealed for 20 min at 650 °C in an H_2 atmosphere to increase the average grain size of the Mo film. Then, 35-nm-thick of periodic plasma-treated SiN_x layer was grown by chemical vapor deposition (CVD) on top of the Mo film as a hard mask, coated first by an amorphous carbon film and then by a metal–organic resist. The resist was patterned using Extreme Ultraviolet (EUV) lithography with periodic 32-nm-wide stripes with a pitch of 64 nm. After SiN_x hard mask opening, the Mo NWs were etched using reactive ion etching (RIE) with a Cl_2/O_2 plasma, stopping on the SiO_2 ESL. Dilute HF solution (0.3% v/v) was applied after the RIE process for 15 s for cleaning. After that, SiO_2 was filled between the Mo NWs using atomic layer deposition (ALD) at 300 °C to reproduce the actual structure of an interconnect layer. The wafer was then polished using chemical mechanical planarization (CMP), and the SiN_x hard mask was selectively removed by RIE. These fabrication steps are summarized in Figure S1 (Supporting Information). Next, individual 5 × 6 mm^2 TEM chips were fabricated using optical lithography patterning and RIE. The backside SiN_x layer served as a hard mask, and the bulk Si was etched with KOH. Finally, the chips were treated with a dilute HF solution (0.25% v/v) to etch away the SiO_2 filling and expose a clean metal surface on the sides of the Mo NWs, as shown in Figure 1B,C. The same chips were used to form the liquid cells shown in Figure 3A. The details of the fabrication steps of the chips and liquid cells are described in our earlier studies.[25,28–30]

Materials: The etching solutions used in this study were prepared from the following chemicals: hydrogen peroxide (30% H_2O_2, Dickson Chemical, Singapore), hydrofluoric acid (48% HF, Cat. No. 695068, Sigma–Aldrich Co. LLC, St. Louis, USA), isopropyl alcohol (IPA, >99.8% Cat. No. 20880.320, VWR International, Radnor, PA, USA). Deionized water with a resistivity of 18.2 MΩ cm was used to prepare all aqueous solutions in this study.

TEM imaging and EELS characterization: A 200 kV JEOL2010F TEM (JEOL Ltd., Tokyo, Japan) equipped with a Gatan OneView camera (Gatan Inc., Pleasanton, CA, USA) was used for both ex situ and in situ TEM imaging. For in situ studies, liquid cells were first assembled using the TEM chips in a custom-built liquid-flow TEM holder.[25,28–30] After inserting the holder into the TEM, the H_2O_2 aqueous solution (1% (v/v)) was introduced into the holder with a syringe pump at a flow rate of 5−10 µL min^{-1}. The in situ image series shown in Figure 3 were recorded at a rate of 10 frames per second with an electron flux of $< 20\ e^-\ Å^{-2}\ s^{-1}$. EELS data was acquired using a 200 kV Thermo Fisher Tecnai G2 TF20 (Thermo Fisher Scientific Ltd., Hillsboro, OR, USA) equipped with a Fischione Model 3000 ADF STEM detector (E.A. Fischione instruments Inc., Export, PA, USA) and GIF Quantum Model 963 EELS detector (Gatan Inc., Pleasanton, CA, USA).

Surface Roughness Quantification: Surface roughness analysis of the top-down TEM images of Mo NWs was performed as follows. The profiles for each NW edge were identified with the canny edge detection algorithm.[44] Then, using low- and high-pass filters in Fourier space, each

profile was decomposed into two components: one with features below 1 nm representing atomic-scale roughness and one with features above 1 nm outlining larger non-uniformities such as grain facets. Importantly, these two profiles sum up to the original edge profile. A standard deviation σ was then computed for each part and called 3σ of the small-scale and large-scale profiles the "roughness" and "waviness", respectively. Again, the sum of these two values equals the standard line-edge roughness (LER) value.[39–42]

Supporting Information

Supporting Information is available from the Wiley Online Library or from the author.

Acknowledgements

This work was supported by the Singapore National Research Foundation's Competitive Research Program funding.

Conflict of Interest

The authors declare no conflict of interest.

Data Availability Statement

The data that support the findings of this study are available from the corresponding author upon reasonable request.

Keywords

cyclic etching, digital etching, liquid cell TEM, metal nanowires, wet etching

Received: September 8, 2023
Revised: November 15, 2023
Published online: December 12, 2023

[1] H. H. Radamson, H. Zhu, Z. Wu, X. He, H. Lin, J. Liu, J. Xiang, Z. Kong, W. Xiong, J. Li, H. Cui, J. Gao, H. Yang, Y. Du, B. Xu, B. Li, X. Zhao, J. Yu, Y. Dong, G. Wang, *Nanomaterials* **2020**, *10*, 1555.
[2] H. Iwai, *Solid-State Electron.* **2015**, *112*, 56.
[3] P. Kapur, J. P. Mcvittie, K. C. Saraswat, *IEEE Trans. Electron Devices* **2002**, *49*, 590.
[4] D. Josell, S. H. Brongersma, Z. Tokei, *Annu. Rev. Mater. Res.* **2009**, *39*, 231.
[5] K. Zhao, Y. Hu, G. Du, Y. Zhao, J. Dong, *Nanomaterials* **2022**, *12*, 1760.
[6] D. Gall, *J. Appl. Phys.* **2020**, *127*, 050901.
[7] D. Gall, *J. Appl. Phys.* **2016**, *119*, 085101.
[8] S. Dutta, K. Sankaran, K. Moors, G. Pourtois, S. Van Elshocht, J. Bömmels, W. Vandervorst, Z. Tokei, C. Adelmann, *J. Appl. Phys.* **2017**, *122*, 025107.
[9] S. Dutta, S. Kundu, A. Gupta, G. Jamieson, J. F. Gomez Granados, J. Bommels, C. J. Wilson, Z. Tokei, C. Adelmann, *IEEE Electron Device Lett.* **2017**, *38*, 949.
[10] K. Motoyama, *2021 IEEE Int. Interconnect Technology Conf. (IITC)*, IEEE, Piscataway, NJ **2021**.
[11] L. Lu, Y. Shen, X. Chen, L. Qian, K. Lu, *Science* **2004**, *304*, 422.
[12] T. Sun, B. Yao, A. P. Warren, K. Barmak, M. F. Toney, R. E. Peale, K. R. Coffey, *Phys. Rev. B* **2010**, *81*, 155454.
[13] P. Y. Zheng, R. P. Deng, D. Gall, *Appl. Phys. Lett.* **2014**, *105*, 131603.
[14] T. Zhou, P. Zheng, S. C. Pandey, R. Sundararaman, D. Gall, *J. Appl. Phys.* **2018**, *123*, 155107.
[15] H. Bishara, S. Lee, T. Brink, M. Ghidelli, G. Dehm, *ACS Nano* **2021**, *15*, 16607.
[16] A. Pacco, T. Nakano, A. Iwasaki, S. Iwahata, E. A. Sanchez, in *2021 IEEE International Interconnect Technology Conference (IITC)*, IEEE, Piscataway, NJ **2021**.
[17] W. Wang, T. Xu, J. Chen, J. Shangguan, H. Dong, H. Ma, Q. Zhang, J. Yang, T. Bai, Z. Guo, H. Fang, H. Zheng, L. Sun, *Nat. Mater.* **2022**, *21*, 859.
[18] M. R. Hauwiller, J. C. Ondry, C. M. Chan, P. Khandekar, J. Yu, A. P. Alivisatos, *J. Am. Chem. Soc.* **2019**, *141*, 4428.
[19] Q. Chen, J. M. Yuk, M. R. Hauwiller, J. Park, K. S. Dae, J. S. Kim, A. P. Alivisatos, *MRS Bull.* **2020**, *45*, 713.
[20] S. J. Park, S.-H. Jo, S. Oh, Y.-S. Oh, S.-J. Kim, H. W. Lee, S.-H. Kang, Y. Hoon Moon, J. Jung, *Mater. Des.* **2022**, *217*, 110631.
[21] S. Paolillo, D. Wan, F. Lazzarino, N. Rassoul, D. Piumi, Z. Tőkei, *J. Vac. Sci. Technol., B* **2018**, *36*, 03E103.
[22] L. G. Bland, K. Gusieva, J. R. Scully, *Electrochim. Acta* **2017**, *227*, 136.
[23] Z. Song, Z.-H. Xie, *Micron* **2018**, *112*, 69.
[24] A. Pacco, Y. Akanishi, Q. T. Le, E. Kesters, G. Murdoch, F. Holsteyns, *Microelectron. Eng.* **2019**, *217*, 111131.
[25] Z. Aabdin, X. M. Xu, S. Sen, U. Anand, P. Král, F. Holsteyns, U. Mirsaidov, *Nano Lett.* **2017**, *17*, 2953.
[26] H.-Y. Ryu, L. Teugels, K. Devriendt, H. Struyf, T.-G. Kim, J.-G. Park, *ECS J. Solid State Sci. Technol.* **2021**, *10*, 094001.
[27] Q.-T. Le, H. Guevenc, A. Ibrahim, A. Klipp, S. Decoster, G. Murdoch, E. A. Sanchez, *ECS Trans.* **2022**, *108*, 39.
[28] Z. Aabdin, T. Ghosh, A. Pacco, S. Raj, H. T. B. Do, K. Saidov, T. W. Weei, U. Anand, P. Král, F. Holsteyns, M. Bosman, U. Mirsaidov, *ACS Appl. Electron. Mater.* **2022**, *4*, 5191.
[29] U. Anand, T. Ghosh, Z. Aabdin, S. Koneti, X. Xu, F. Holsteyns, U. Mirsaidov, *Proc. Natl. Acad. Sci. U. S. A.* **2021**, *118*, e2108074118.
[30] U. Anand, T. Ghosh, Z. Aabdin, N. Vrancken, H. Yan, X. Xu, F. Holsteyns, U. Mirsaidov, *ACS Appl. Nano Mater.* **2021**, *4*, 2664.
[31] R. Mahjoub, M. Ferry, N. Stanford, *Comput. Mater. Sci.* **2022**, *210*, 111042.
[32] Q. Zhu, Z. Pan, Z. Zhao, G. Cao, L. Luo, C. Ni, H. Wei, Z. Zhang, F. Sansoz, J. Wang, *Nat. Commun.* **2021**, *12*, 558.
[33] H. Philipsen, N. Mouwen, S. Teck, W. Monnens, Q. T. Le, F. Holsteyns, H. Struyf, *Electrochim. Acta* **2019**, *306*, 285.
[34] A. C. West, H. Deligianni, P. C. Andricacos, *IBM J. Res. Dev.* **2005**, *49*, 37.
[35] M. Windholz, *The Merck index : an encyclopedia of chemicals, drugs, and biologicals*, Merck and Co., Rahway, NJ **1983**.
[36] K.-H. Tytko, in *Mo Molybdenum: Molybdenum Oxide Hydrates*, (Eds.: K.-H. Tytko, H. Katscher, F. Schröder), Springer, Berlin, Germany **1986**.
[37] M. P. Mitoraj, A. Michalak, *Struct. Chem.* **2012**, *23*, 1369.
[38] I. A. De Castro, R. S. Datta, J. Z. Ou, A. Castellanos-Gomez, S. Sriram, T. Daeneke, K. Kalantar-Zadeh, *Adv. Mater.* **2017**, *29*, 1701619.
[39] R. A. Lawson, A. P. G. Robinson, in *Materials and Processes for Next Generation Lithography*, Elsevier, Amsterdam, The Netherlands **2016**, pp. 1–90.
[40] S. G. Yazgi, T. Ivanov, M. Holz, I. W. Rangelow, B. E. Alaca, *J. Vac. Sci. Technol., B* **2020**, *38*, 012602.
[41] W. Steinhögl, G. Schindler, G. Steinlesberger, M. Traving, M. Engelhardt, *Microelectron. Eng.* **2004**, *76*, 126.
[42] G. P. Patsis, V. Constantoudis, A. Tserepi, E. Gogolides, G. Grozev, *J. Vac. Sci. Technol., B* **2003**, *21*, 1008.
[43] S. S. N. Murthy, *J. Phys. Chem. A* **1999**, *103*, 7927.
[44] G. Bradski, *J. Softw. Tools* **2000**, *120*, 122.